

Charge transport in oxygen-deficient EuTiO_3 : The emerging picture of dilute metallicity in quantum-paraelectric perovskite oxides

Johannes Engelmayr,¹ Xiao Lin,^{1,*} Christoph P. Grams,¹ Raphael German,¹ Tobias Fröhlich,¹ Joachim Hemberger,¹ Kamran Behnia,^{2,†} and Thomas Lorenz^{1,‡}

¹*II. Physikalisches Institut, Universität zu Köln, Zùlpicher Straße 77, 50937 Köln, Germany*

²*Laboratoire de Physique et d'Étude des Matériaux (UMR 8213 CNRS-ESPCI), PSL Research University, 10 Rue Vauquelin, 75005 Paris, France*



(Received 13 February 2019; published 2 May 2019)

We report on a study of charge transport in $\text{EuTiO}_{3-\delta}$ single crystals with carrier density tuned across several orders of magnitude. Comparing this system with other quasicubic perovskites, in particular strontium titanate, we draw a comprehensive picture of metal-insulator transition and dilute metallicity in this ABO_3 family. Because of a lower electric permittivity, the metal-insulator transition in $\text{EuTiO}_{3-\delta}$ occurs at higher carrier densities compared to SrTiO_3 . At low temperature, a distinct T^2 resistivity is visible. Its prefactor A smoothly decreases with increasing carrier concentration in a similar manner in three different perovskites. Our results draw a comprehensive picture of charge transport in doped quantum paraelectrics.

DOI: 10.1103/PhysRevMaterials.3.051401

During the last decade, the metal-insulator transition (MIT) in weakly doped SrTiO_3 has attracted renewed interest. The pure compound is a highly insulating quantum paraelectric [1], which on the one hand becomes ferroelectric by a partial substitution of Sr by Ca ($\text{Sr}_{1-x}\text{Ca}_x\text{TiO}_3$, $0.002 \leq x \leq 0.12$) [2,3]. On the other hand, it becomes metallic upon reduction ($\text{SrTiO}_{3-\delta}$) [4] and even superconducting [5] at remarkably low carrier concentrations, which identified SrTiO_3 as the most dilute superconductor [6]. Furthermore, a ferroelectriclike transition inside the superconducting phase has been observed in compounds with both Ca substitution and oxygen vacancies ($\text{Sr}_{1-x}\text{Ca}_x\text{TiO}_{3-\delta}$) [7]. Apart from reduction, SrTiO_3 has been subjected to other variants of n -type doping by, e.g., substituting Ti^{4+} with Nb^{5+} ($\text{SrTi}_{1-x}\text{Nb}_x\text{O}_3$) [4,8–10], or Sr^{2+} with La^{3+} ($\text{Sr}_{1-x}\text{La}_x\text{TiO}_3$) [10–13]. In all three cases a T^2 behavior of the resistivity is found [14–16]. For many systems, the prefactor A of $\rho(T) = \rho_0 + AT^2$ is related to the electronic specific heat coefficient γ , since both depend on the Fermi energy E_F , as is expressed in the Kadowaki-Woods ratio A/γ^2 [17]. Furthermore, E_F itself depends on the carrier density n and one may expect a particular scaling behavior in $A(n)$ as shown for metallic $\text{SrTiO}_{3-\delta}$ [16,18].

In order to investigate these phenomena in other systems, EuTiO_3 is a prime candidate, because both materials are similar in many aspects. Sr^{2+} and Eu^{2+} have almost the same ionic radius [19]. Both compounds have the ideal cubic perovskite structure (space group $Pm\bar{3}m$) at room temperature and undergo a structural phase transition to tetragonal ($I4/mcm$) upon cooling [20,21], and both are quantum paraelectrics [1,22,23]. Nevertheless, there are also clear differ-

ences. SrTiO_3 crystals are transparent, whereas EuTiO_3 is black, which can be understood from band-structure calculations yielding a band gap of 1 eV [24], whereas SrTiO_3 has a gap of 3.2 eV [25]. SrTiO_3 is nonmagnetic in contrast to EuTiO_3 where Eu^{2+} has a large, local magnetic moment of $7\mu_B$. These moments order antiferromagnetically below $T_N = 5.5$ K in a G -type configuration [26,27].

The research on n -doped EuTiO_3 is sparse. To our knowledge only five publications exist: One report deals with poly- and single-crystalline $\text{EuTi}_{1-x}\text{Nb}_x\text{O}_3$ with $x \leq 0.3$ [28] and another two with single-crystalline $\text{Eu}_{1-x}\text{La}_x\text{TiO}_3$ ($x \leq 0.1$ [29,30]). Studies of oxygen-deficient EuTiO_3 are restricted to ceramics [31] and thin films [32]. Here, we present a detailed study of single-crystalline $\text{EuTiO}_{3-\delta}$ tuned from semiconducting to metallic via reduction. We derive the electron mobility and discuss its temperature dependence in comparison to that of SrTiO_3 . We find an AT^2 resistivity behavior of metallic $\text{EuTiO}_{3-\delta}$ where A systematically decreases with increasing charge-carrier content, which is discussed in a larger context of charge transport in weakly doped perovskite oxides.

The EuTiO_3 crystals were grown by the floating-zone technique. We used polycrystalline powders of Eu_2O_3 (chemical purity 99.99%), TiO (99.5%), and TiO_2 (99.99%) as starting materials. The powders were mixed for 1 h and the mixture was pressed to a cylindrical rod at 50 MPa. In order to avoid emergence of Eu^{3+} via oxygen capture, we skipped preliminary powder reactions and put the pressed rod directly into the floating-zone system. Centimeter-sized single crystals were grown in argon atmosphere using a growth speed of 10 mmh^{-1} and a relative rotation of the rods of 30 rpm. X-ray powder diffraction measurements verified phase purity and Laue images confirmed single crystallinity.

The as-grown crystal was cut into cuboid pieces with all faces being $\{100\}$ planes. In order to induce electron doping, the samples were annealed in sealed fused-quartz tubes with

*Present address: School of Science, Westlake University, 18 Shilongshan Road, 310024 Hangzhou, China.

†tl@ph2.uni-koeln.de

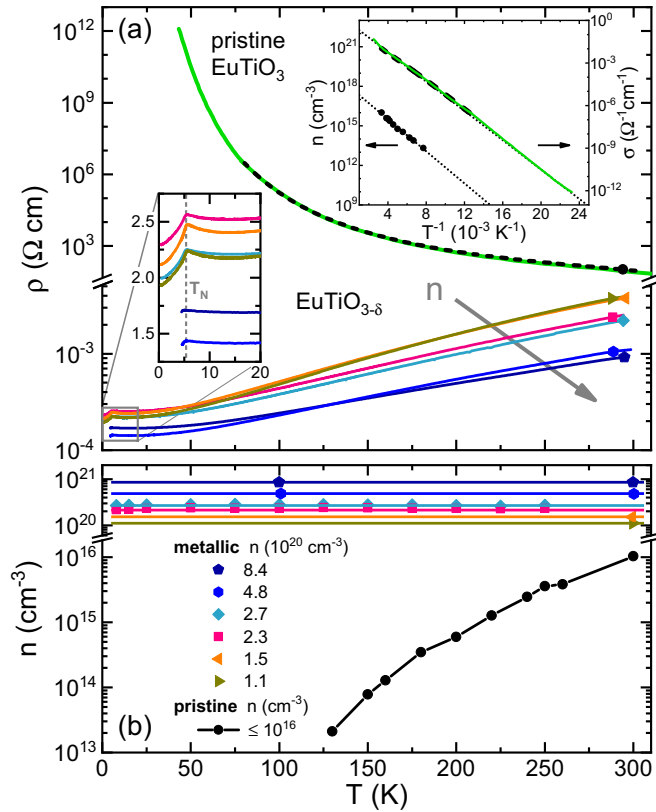


FIG. 1. (a) Resistivity $\rho(T)$ of semiconducting pristine EuTiO_3 determined by dc measurements (black dashed line) and dielectric spectroscopy (green solid line) in comparison to metallic $\text{EuTiO}_{3-\delta}$ which were cut from the same single crystal and oxygen reduced. (b) Charge-carrier concentrations n of all samples deduced from Hall effect measurements at various temperatures. The upper inset in (a) shows Arrhenius plots of $n(T)$ and of the conductivity $\sigma(T)$ together with linear fits (dotted lines). The lower inset is an enlarged view of the $\rho(T)$ anomalies at $T_N = 5.5 \text{K}$, which is n independent, in agreement with a previous report [31]. Note the scale breaks in both main panels.

low argon pressure ($\lesssim 10^{-5}$ mbar) and titanium metal powder (99.99%) acting as oxygen catcher. The quartz tubes were heated for 10 h at temperatures between 650°C and 850°C depending on the intended carrier concentration. In order to have an indicator for homogeneity, in each run two samples with different thicknesses (0.2 and 0.4 mm) were annealed simultaneously in the same quartz tube. Resistivity and Hall effect measurements were carried out by a standard four-probe and six-probe method, respectively, using a home-built dipstick setup and a commercial ^3He insert (Heliox, Oxford Instruments) for wet cryostats.

Figure 1 shows the resistivity ρ and charge-carrier density n as a function of temperature—both in semilogarithmic scales—for different $\text{EuTiO}_{3-\delta}$ samples. In contrast to SrTiO_3 , which is highly insulating, the dc conductivity of pristine EuTiO_3 is measurable down to about 80 K [Fig. 1(a)] and is complemented with dielectric spectroscopy measurements (see Appendix) to even lower temperature. Its carrier density obtained from Hall effect measurements [Fig. 1(b)] is temperature dependent and ranges from $n = 10^{16} \text{cm}^{-3}$ at room

temperature down to $n \approx 10^{13} \text{cm}^{-3}$ at the lowest measurable temperature ($\approx 130 \text{K}$). The activated behavior is clearly seen in the Arrhenius plots of both conductivity and carrier density (upper inset of Fig. 1). The corresponding fits yield very similar activation energies (100 meV from conductivity and 120 meV from carrier density), but both are much smaller than the theoretically expected intrinsic band gap of 1 eV [24] meaning that the pristine EuTiO_3 is weakly impurity doped.

To induce a MIT, the aforementioned annealing technique is used. Annealing temperatures below 600°C seem to have no effect on the oxygen content, since the $\rho(T)$ curves remain unchanged (not shown). For annealing temperatures above 750°C we obtain metallic samples with temperature-independent carrier densities that cover a range of 10^{20}cm^{-3} to 10^{21}cm^{-3} (see Fig. 1). Above 130 K the $\rho(T)$ curves are ordered by carrier density, i.e., σ increases upon increasing n and, in reverse, the $n(T)$ curves are ordered by the high-temperature conductivity. At low temperatures, some of the $\rho(T)$ curves are crossing each other, which may partly arise from different residual resistivities and/or some uncertainty in determining the exact geometries. For annealing temperatures $600^\circ\text{C} < T_{\text{ann}} < 750^\circ\text{C}$, the simultaneously annealed samples of different thicknesses show large deviations in both $\rho(T)$ and n . This indicates inhomogeneous charge-carrier concentrations and thus these samples are not taken into account here. In this context, it is worth mentioning that a certain gradient in the oxygen-defect concentration is naturally expected for postannealed single crystals. However, above a certain critical concentration the wave functions of the induced charge carriers overlap sufficiently and a metallic state with an averaged homogeneous charge-carrier density results.

The absence of homogeneous samples between pristine and metallic $\text{EuTiO}_{3-\delta}$ hinders an exact determination of the MIT. The lowest carrier density of 10^{20}cm^{-3} yields an upper boundary for the critical carrier density n_c of the MIT and is about four orders of magnitude larger than the corresponding one ($\approx 10^{16} \text{cm}^{-3}$) of SrTiO_3 [4]. This difference can be understood by comparing the permittivities ϵ of EuTiO_3 and SrTiO_3 . While SrTiO_3 has an extremely large ϵ of roughly 20 000 at low temperatures [1], that of EuTiO_3 is smaller by a factor of 50. We find $\epsilon \approx 400$ (see Appendix) in agreement with previous single-crystal data [22], whereas smaller values are reported for ceramics [23,33].

Of course, these values were obtained for pristine EuTiO_3 . For doped samples, one defines an effective Bohr radius $a_B^* = a_B \epsilon m_e / m^*$, which renormalizes $a_B \approx 0.5 \text{\AA}$ of the hydrogen atom by taking into account the permittivity ϵ and the band mass m^* . The so-called Mott criterion [34] compares a_B^* as a measure for the overlap of the electronic wave functions to the average distance between donor atoms $n^{-1/3}$. The huge low-temperature ϵ of SrTiO_3 results in an effective Bohr radius of about 6700 \AA , compared to $a_B^* \approx 130 \text{\AA}$ for EuTiO_3 . Here, we use $m^* = 1.5m_e$ as determined for the lowest lying conduction band of $\text{SrTiO}_{3-\delta}$ [35] for both SrTiO_3 and EuTiO_3 . The much smaller value of a_B^* explains that n_c of EuTiO_3 is about four orders of magnitude larger than that of SrTiO_3 . In passing, we also note that the influence of the above-mentioned inhomogeneities in the oxygen-defect concentrations is suppressed more rapidly with increasing

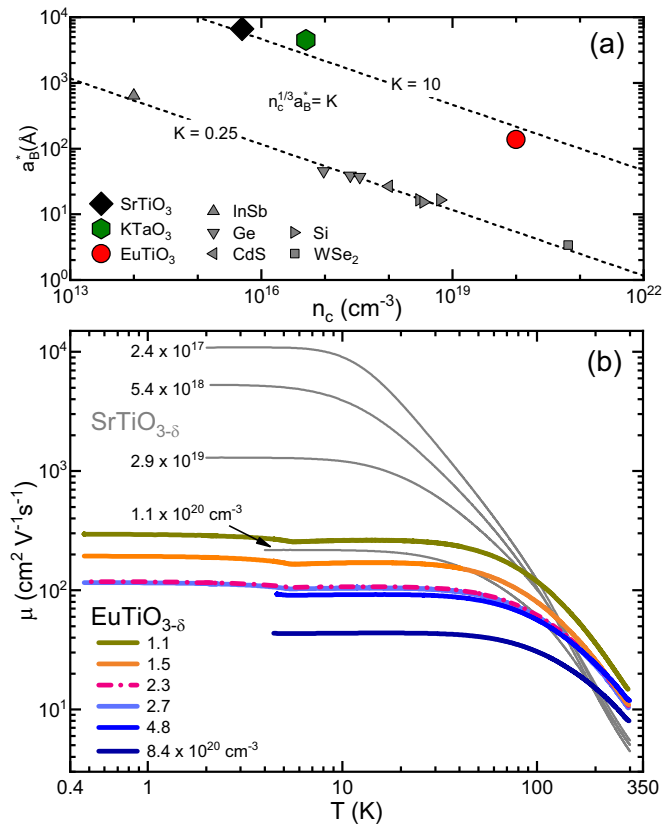


FIG. 2. (a) Effective Bohr radius a_B^* versus critical charge-carrier density n_c of various doped semiconductors (taken from [36]) in comparison to the observed MIT of $\text{EuTiO}_{3-\delta}$ and related doped oxides SrTiO_3 [4] and KTaO_3 [38,39]. Dashed lines represent the scaling behavior $n_c^{1/3} a_B^* = K$ with different values of K . (b) Mobility $\mu(T, n)$ of the metallic $\text{EuTiO}_{3-\delta}$ samples in comparison to that of $\text{SrTiO}_{3-\delta}$.

a_B^* . Figure 2(a) shows the scaling behavior $n_c^{1/3} a_B^* = K$ as dashed lines for different values of K . Experiments on doped semiconductors have detected a sharp MIT at a critical density of n_c and the available data follows a scaling relation with $K = 0.25$ [36,37], which corresponds to the so-called Mott criterion [34]. In perovskite oxides, there is no experimental data resolving a sharp MIT at n_c and metallicity is observed in EuTiO_3 , SrTiO_3 [4], and KTaO_3 [38,39] at carrier densities which are much larger than expected according to the Mott criterion. Nevertheless, these carrier densities scale with a_B^* .

Figure 2(b) displays the mobility $\mu = 1/(ne\rho)$ of metallic $\text{EuTiO}_{3-\delta}$ as a function of temperature in double-logarithmic scales. Below 40 K all $\mu(T)$ curves approach constant values, which are ordered by carrier density n , i.e., $\mu(n)$ systematically decreases with increasing n . The additional kinks result from the magnetic order at $T_N = 5.5$ K as already shown in Fig. 1(a) for $\rho(T)$. In the high-temperature regime, the mobility curves decrease due to increasing electron-phonon scattering and seem to approach an n -independent power law. Such a behavior has been already observed in SrTiO_3 [40]. For comparison, we also show the mobility data of four $\text{SrTiO}_{3-\delta}$ crystals with $10^{17} \text{ cm}^{-3} \leq n \lesssim 10^{20} \text{ cm}^{-3}$. Because $\text{SrTiO}_{3-\delta}$ is already metallic for very low carrier densities,

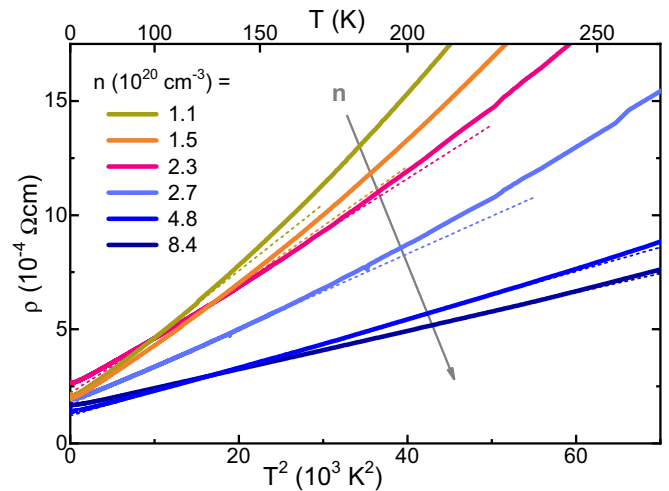


FIG. 3. Resistivity ρ of $\text{EuTiO}_{3-\delta}$ as a function of T^2 . The dashed lines are fits of the form $\rho(T) = \rho_0 + AT^2$. With increasing n the prefactor A decreases and the temperature range of the T^2 behavior increases.

higher mobilities than in $\text{EuTiO}_{3-\delta}$ are reached in the low-temperature regime, but even across both compounds all curves remain ordered by increasing n . Toward high temperature, the mobility curves $\mu(T, n)$ of $\text{SrTiO}_{3-\delta}$ merge and fall below those of EuTiO_3 above about 200 K. This is surprising in view of the structural phase transition of EuTiO_3 , which is in that temperature range [20,31]. In contrast, the transition in $\text{SrTiO}_{3-\delta}$ appears at $T_s \simeq 105$ K [1,41] and linearly decreases with increasing charge-carrier content [42]. Using x-ray- and Raman-scattering measurements, we derive $T_s \simeq 260$ K on our pristine EuTiO_3 and $T_s \simeq 200$ K for the highest $n = 8.4 \times 10^{20} \text{ cm}^{-3}$ (to be published elsewhere). However, neither $\text{SrTiO}_{3-\delta}$ nor $\text{EuTiO}_{3-\delta}$ show any anomalies in the mobility data reflecting the structural transitions. Recently, both the magnitude and temperature dependence of the mobility in $\text{SrTiO}_{3-\delta}$ have attracted attention [43,44]. Mischenko *et al.* [43] argue that a polaronic approach can lead to a scattering rate larger than the thermal energy of carriers in agreement with the data. *Ab initio* calculations by Zhou *et al.* [44] reproduce the experimentally observed T^{-3} temperature dependence of the mobility of $\text{SrTiO}_{3-\delta}$ [40], but the calculated absolute value is an order of magnitude larger than the experimental data. Moreover, in these theoretical approaches the antiferrodistortive soft mode does not play a key role, in agreement with the absence of anomalies in the measured mobility data.

Figure 3 shows the resistivity ρ as a function of T^2 together with fits of the form $\rho(T) = \rho_0 + AT^2$ (dashed lines). The fits deviate from the data for high temperatures and with increasing carrier density the temperature range of the T^2 behavior systematically increases, which is in agreement with the findings for $\text{SrTiO}_{3-\delta}$ [16]. In $\text{EuTiO}_{3-\delta}$ we have an additional deviation at low temperatures that is related to the magnetic transition at $T_N = 5.5$ K. Figure 4(a) shows the prefactor A from these fits as a function of n in double-logarithmic scales. Here, we compare $A(n)$ for $\text{EuTiO}_{3-\delta}$ to that of $\text{SrTiO}_{3-\delta}$, $\text{Sr}_{1-x}\text{La}_x\text{TiO}_3$, and $\text{SrTi}_{1-x}\text{Nb}_x\text{O}_3$ [14–16],

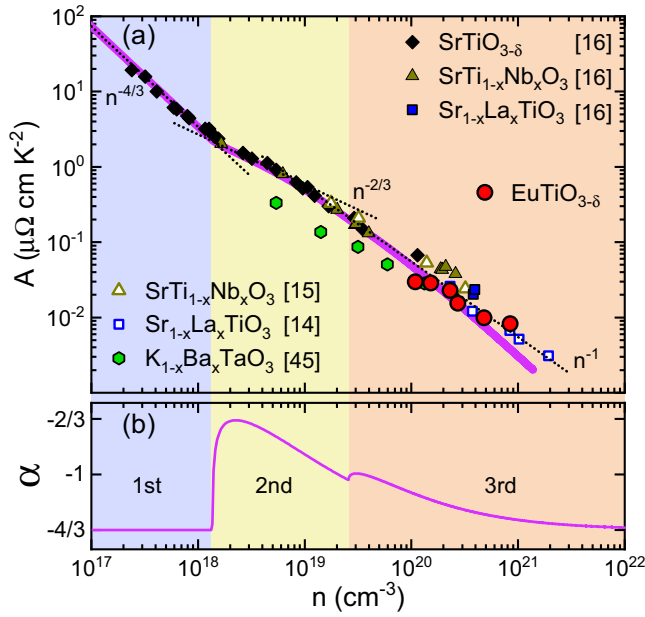


FIG. 4. (a) Prefactor of the AT^2 resistivity versus carrier concentration n in doped perovskites EuTiO_3 , SrTiO_3 [14–16], and KTaO_3 [45]. Dotted black lines are guides to the eye. The thick line in (a) represents $A(n)$ calculated for a three-band model; the corresponding exponent α of $A \propto n^\alpha$ is shown in (b) (see text for details). Color boundaries indicate band edges of doped SrTiO_3 [35].

and we also include $A(n)$ of the nontitanate perovskite $\text{K}_{1-x}\text{Ba}_x\text{TaO}_3$ [45]. All titanate systems follow a general trend as is marked by dotted black lines, which are guides to the eye and indicate power laws $A \propto n^\alpha$ with $\alpha = -4/3, -2/3, -1$. Band-structure calculations for n -doped SrTiO_3 [15] yield a model with three bands that are filled consecutively with increasing n . The critical carrier densities n_{c1} (n_{c2}), at which the filling of the second (third) band sets in, are known from experiments [35] and illustrated by background-color boundaries. Below n_{c1} , where only the first band is filled, a power law $n^{-4/3}$ is seen as is expected for a single parabolic band with $E_F \propto n^{2/3}$ and a simple $A \propto E_F^{-2}$ relation. When the second band starts to be filled at n_{c1} , the exponent α of $A \propto n^\alpha$ suddenly increases and finally approaches -1 , which does not change much above n_{c2} .

The increase of α is a natural consequence of a three-band system. If we consider the most simple case of three parabolic bands with band minima at energies E_i , effective masses m_i , and densities of states $g_i(E) \propto m_i^{3/2} \sqrt{E - E_i}$, then each band contributes

$$n_i(E_F) = \frac{1}{3\pi^2} \left(\frac{2m_i}{\hbar^2} \right)^{3/2} \int_{E_i}^{E_F} \sqrt{E - E_i} dE \quad (1)$$

to the total electron density $n(E_F) = \sum_i n_i(E_F)$. We use the band masses $m_0 = m_2 = 1.5m_e$ and $m_1 = 3.5m_e$ from Shubnikov–de Haas measurements of $\text{SrTiO}_{3-\delta}$ [35] and adjust $E_{1,2}$ to 2 and 10 meV, respectively, to match the experimental critical carrier densities [46]. From the inverse function $E_F(n)$ we calculate $A(n) \propto E_F^{-2}(n)$ which describes the data of the doped titanates over almost the entire range of n , as is shown by the thick line in Fig. 4(a). This also holds for

the exponent α of $A \propto n^\alpha$ obtained from the slope of $\log A$ vs $\log n$ [Fig. 4(b)]. In view of the simple model, which neglects deviations from the parabolic band shapes as well as their anisotropy, this good agreement with the experimental data is remarkable. The available $A(n)$ data of the nontitanate perovskite $\text{K}_{1-x}\text{Ba}_x\text{TaO}_3$ [45] fit into this picture as well, because this material has lower effective masses ($0.55\text{--}0.8m_e$) [39]. Consequently, at a given carrier concentration n , the Fermi energy is larger and the prefactor A is lower compared to the titanates. A more sophisticated theoretical treatment could provide a generalized uniform description of the $A(n)$ behavior for an even larger variety of metallic perovskite oxides with low carrier densities.

In summary, we present a detailed report of the metal-insulator transition in oxygen-deficient single-crystalline EuTiO_3 , which shows many similarities with that in SrTiO_3 . However, it sets in at a much higher carrier concentration (factor 10^4), which results from the smaller permittivity of EuTiO_3 , implying a smaller effective Bohr radius a_B^* , i.e., a smaller overlap of the electronic wave functions. We show that metallicity in three perovskite oxides scales with the effective Bohr radius a_B^* , but it emerges at a carrier density much larger than suggested by the Mott criterion. The low-temperature mobility of metallic EuTiO_3 and SrTiO_3 systematically increases with decreasing charge-carrier concentration across both materials. We find an AT^2 behavior in $\rho(T)$ of metallic $\text{EuTiO}_{3-\delta}$ where the prefactor $A(n)$ systematically decreases with increasing charge-carrier density n and even quantitatively agrees with $A(n)$ of doped SrTiO_3 . This general behavior of $A(n)$ can be described within a three-band model.

We acknowledge support by the DFG (German Research Foundation) via Project No. 277146847 within CRC 1238 (subprojects A02, B01, B02, and B03). This work is part of a DFG-ANR project funded by Agence Nationale de la Recherche (ANR-18-CE92-0020-01) and by the DFG through projects LO 818/6-1 and HE 3219/6-1. X.L. acknowledges support by the Alexander von Humboldt Foundation and Zhejiang Provincial Natural Science Foundation of China under Grant No. LQ19A040005.

APPENDIX: DIELECTRIC SPECTROSCOPY

The dielectric and transport properties of pristine EuTiO_3 toward higher resistivities were determined by contact-based impedance spectroscopy. These measurements were performed in a commercial ^4He -flow cryo-magnet (Quantum Design PPMS) on crystals in capacitor geometry with metallized surfaces $A \approx 4 \text{ mm}^2$ and thickness $d \approx 0.5 \text{ mm}$ along a cubic [100] axis. We used a high-impedance frequency response analyzer (Novocontrol) and a vector network analyzer (ZNB8, Rohde & Schwarz) to cover a joint frequency range $1 \text{ Hz} \leq \nu \leq 100 \text{ MHz}$ with voltage stimulation below 1 V_{rms} .

As expected for semiconductors, Schottky-type depletion layers at the contact interfaces cause a capacitive contribution C_C , which together with the contact resistance R_C form an RC element in series with the intrinsic sample impedance. This gives rise to Maxwell-Wagner-type relaxational effects [48], but for frequencies $2\pi\nu > 1/R_C C_C$ the

contacts effectively are short-circuited [49,50]. The crossover from contact-dominated to intrinsic response is clearly seen in the permittivity ε as well as in the conductivity σ . The low- T /high- ν limit of the frequency- and temperature-dependent data represents the intrinsic quasistatic ε [Fig. 5(a)]. The corresponding intrinsic σ , marked in green in Fig. 5(b) agrees well with the inverse dc resistivity $1/\rho_{dc}$ [see Fig. 1(a)].

EuTiO₃ is a quantum paraelectric where long-range order is prevented by quantum fluctuations. The fingerprint of quantum-paraelectric behavior is a Curie-like rise of the permittivity with decreasing temperature followed by a saturation at an elevated $\varepsilon(T \rightarrow 0)$, which can be modeled by the well-known Barrett formula [47]

$$\varepsilon(T) = \frac{C}{(T_{\Omega}/2) \coth(T_{\Omega}/2T) - T_0} + \varepsilon_{\infty}. \quad (\text{A1})$$

Here, T_{Ω} represents the influence of quantum fluctuations and T_0 is the paraelectric Curie temperature. The fit of the high-frequency data of $\varepsilon(T < 200 \text{ K})$ reveals $T_{\Omega} \simeq 160 \text{ K}$ and $T_0 \simeq -190 \text{ K}$. The value of T_{Ω} agrees with a previous report [22] and, remarkably, it is four times larger compared to SrTiO₃ [1,51] indicating much stronger quantum fluctuations in EuTiO₃. Our T_0 value differs in magnitude from [22] where a considerably smaller temperature range could be evaluated, but is also negative denoting rather antiferroelectric correlations in EuTiO₃. As shown in the inset of Fig. 5(a), $\varepsilon(T)$ has a clear anomaly at $T_N = 5.5 \text{ K}$, which results from a significant magnetoelectric coupling [22].

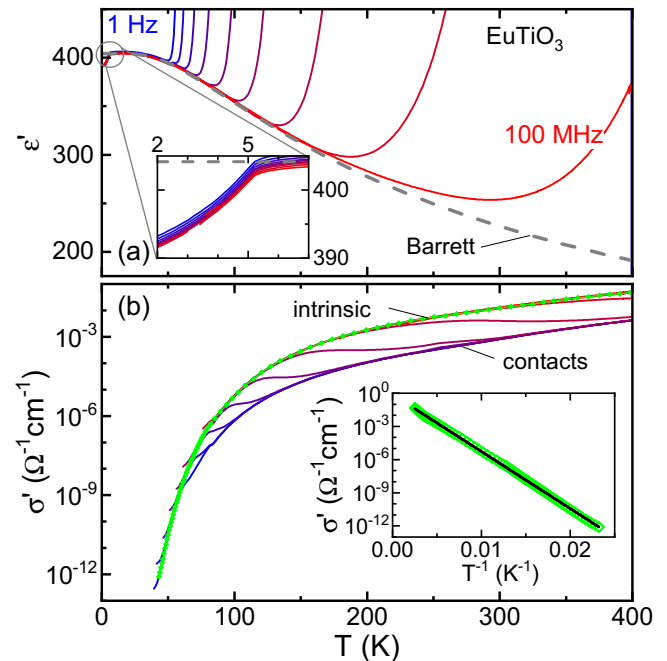


FIG. 5. (a) Temperature-dependent ε' measured for frequencies $1 \text{ Hz} \leq \nu \leq 100 \text{ MHz}$. The steep rise of $\varepsilon'(T, \nu)$ for high- T /low- ν results from contact contributions. The intrinsic low- T /high- ν behavior of $\varepsilon'(T, \nu)$ is fitted via the Barrett formula (dashed line) [47]. The inset shows the anomaly of $\varepsilon'(T, \nu)$ at $T_N = 5.5 \text{ K}$. (b) Corresponding conductivity data $\sigma'(T)$. The inset shows an Arrhenius plot of the intrinsic $\sigma'(T)$ with a linear fit (black line).

- [1] K. A. Müller and H. Burkard, SrTiO₃: An intrinsic quantum paraelectric below 4 K, *Phys. Rev. B* **19**, 3593 (1979).
- [2] J. G. Bednorz and K. A. Müller, Sr_{1-x}Ca_xTiO₃: An XY Quantum Ferroelectric with Transition to Randomness, *Phys. Rev. Lett.* **52**, 2289 (1984).
- [3] B. S. de Lima, M. S. da Luz, F. S. Oliveira, L. M. S. Alves, C. A. M. dos Santos, F. Jomard, Y. Sidis, P. Bourges, S. Harms, C. P. Grams, J. Hemberger, X. Lin, B. Fauqué, and K. Behnia, Interplay between antiferrodistortive, ferroelectric, and superconducting instabilities in Sr_{1-x}Ca_xTiO_{3-δ}, *Phys. Rev. B* **91**, 045108 (2015).
- [4] A. Spinelli, M. A. Torija, C. Liu, C. Jan, and C. Leighton, Electronic transport in doped SrTiO₃: Conduction mechanisms and potential applications, *Phys. Rev. B* **81**, 155110 (2010).
- [5] J. F. Schooley, W. R. Hosler, and M. L. Cohen, Superconductivity in Semiconducting SrTiO₃, *Phys. Rev. Lett.* **12**, 474 (1964).
- [6] X. Lin, Z. Zhu, B. Fauqué, and K. Behnia, Fermi Surface of the Most Dilute Superconductor, *Phys. Rev. X* **3**, 021002 (2013).
- [7] C. W. Rischau, X. Lin, C. P. Grams, D. Finck, S. Harms, J. Engelmayer, T. Lorenz, Y. Gallais, B. Fauqué, J. Hemberger, and K. Behnia, A ferroelectric quantum phase transition inside the superconducting dome of Sr_{1-x}Ca_xTiO_{3-δ}, *Nat. Phys.* **13**, 643 (2017).
- [8] C. S. Koonce, M. L. Cohen, J. F. Schooley, W. R. Hosler, and E. R. Pfeiffer, Superconducting Transition Temperatures of Semiconducting SrTiO₃, *Phys. Rev.* **163**, 380 (1967).
- [9] G. Binnig, A. Baratoff, H. E. Hoening, and J. G. Bednorz, Two-Band Superconductivity in Nb-Doped SrTiO₃, *Phys. Rev. Lett.* **45**, 1352 (1980).
- [10] S. Ohta, T. Nomura, H. Ohta, and K. Koumoto, High-temperature carrier transport and thermoelectric properties of heavily La- or Nb-doped SrTiO₃ single crystals, *J. Appl. Phys.* **97**, 034106 (2005).
- [11] K. Uematsu, O. Sakurai, N. Mizutani, and M. Kato, Electrical properties of La-doped SrTiO₃ (La: 0.1 to 2.0 at %) single crystals grown by xenon-arc image floating zone method, *J. Mater. Sci.* **19**, 3671 (1984).
- [12] C. Q. Tang, Z. Xia, S. Yao, and S. Chen, Dependence of the electric properties and the positron lifetimes on the dopant content in La-doped SrTiO₃, *Cryst. Res. Technol.* **31**, 821 (1996).
- [13] H. Suzuki, H. Bando, Y. Ootuka, I. H. Inoue, T. Yamamoto, K. Takahashi, and Y. Nishihara, Superconductivity in single-crystalline Sr_{1-x}La_xTiO₃, *J. Phys. Soc. Jpn.* **65**, 1529 (1996).
- [14] T. Okuda, K. Nakanishi, S. Miyasaka, and Y. Tokura, Large thermoelectric response of metallic perovskites: Sr_{1-x}La_xTiO₃ (0 ≤ x ≤ 0.1), *Phys. Rev. B* **63**, 113104 (2001).
- [15] D. van der Marel, J. L. M. van Mechelen, and I. I. Mazin, Common Fermi-liquid origin of T² resistivity and superconductivity in SrTiO₃, *Phys. Rev. B* **84**, 205111 (2011).

- [16] X. Lin, B. Fauqué, and K. Behnia, Scalable T^2 resistivity in a small single-component Fermi surface, *Science* **349**, 945 (2015).
- [17] K. Kadowaki and S. B. Woods, Universal relationship of the resistivity and specific heat in heavy-Fermion compounds, *Solid State Commun.* **58**, 507 (1986).
- [18] E. Mikheev, S. Raghavan, J. Y. Zhang, P. B. Marshall, A. P. Kajdos, L. Balents, and S. Stemmer, Carrier density independent scattering rate in SrTiO₃-based electron liquids, *Sci. Rep.* **6**, 20865 (2016).
- [19] In Shannon's paper of ionic radii [52] no value is given for the ionic radius of Eu²⁺ with a 12-fold coordination, but it is pointed out that the radius of Eu²⁺ is only slightly larger than that of Sr²⁺ for all coordination numbers. This is supported by the fact that the lattice parameters of both compounds are almost the same [53].
- [20] A. Bussmann-Holder, J. Köhler, R. K. Kremer, and J. M. Law, Relation between structural instabilities in EuTiO₃ and SrTiO₃, *Phys. Rev. B* **83**, 212102 (2011).
- [21] M. Allietta, M. Scavini, L. J. Spalek, V. Scagnoli, H. C. Walker, C. Panagopoulos, S. S. Saxena, T. Katsufuji, and C. Mazzoli, Role of intrinsic disorder in the structural phase transition of magnetoelectric EuTiO₃, *Phys. Rev. B* **85**, 184107 (2012).
- [22] T. Katsufuji and H. Takagi, Coupling between magnetism and dielectric properties in quantum paraelectric EuTiO₃, *Phys. Rev. B* **64**, 054415 (2001).
- [23] S. Kamba, D. Nuzhnyy, P. Vaněk, M. Savinov, K. Knížek, Z. Shen, E. Šantavá, K. Maca, M. Sadowski, and J. Petzelt, Magnetodielectric effect and optic soft mode behaviour in quantum paraelectric EuTiO₃ ceramics, *Europhys. Lett.* **80**, 27002 (2007).
- [24] H. Akamatsu, Y. Kumagai, F. Oba, K. Fujita, H. Murakami, K. Tanaka, and I. Tanaka, Antiferromagnetic superexchange via 3d states of titanium in EuTiO₃ as seen from hybrid Hartree-Fock density functional calculations, *Phys. Rev. B* **83**, 214421 (2011).
- [25] D. Bäuerle, W. Braun, V. Saile, G. Sprüssel, and E. E. Koch, Vacuum ultraviolet reflectivity and band structure of SrTiO₃ and BaTiO₃, *Z. Phys. B* **29**, 179 (1978).
- [26] T. R. McGuire, M. W. Shafer, R. J. Joenk, H. A. Alperin, and S. J. Pickart, Magnetic structure of EuTiO₃, *J. Appl. Phys.* **37**, 981 (1966).
- [27] V. Scagnoli, M. Allietta, H. Walker, M. Scavini, T. Katsufuji, L. Sagarna, O. Zaharko, and C. Mazzoli, EuTiO₃ magnetic structure studied by neutron powder diffraction and resonant x-ray scattering, *Phys. Rev. B* **86**, 094432 (2012).
- [28] L. Li, J. R. Morris, M. R. Koehler, Z. Dun, H. Zhou, J. Yan, D. Mandrus, and V. Keppens, Structural and magnetic phase transitions in EuTi_{1-x}Nb_xO₃, *Phys. Rev. B* **92**, 024109 (2015).
- [29] T. Katsufuji and Y. Tokura, Transport and magnetic properties of a ferromagnetic metal: Eu_{1-x}R_xTiO₃, *Phys. Rev. B* **60**, R15021 (1999).
- [30] Y. Tomioka, T. Ito, and A. Sawa, Magnetotransport properties of Eu_{1-x}La_xTiO₃ (0 ≤ x ≤ 0.07) single crystals, *J. Phys. Soc. Jpn.* **87**, 094716 (2018).
- [31] B. J. Kennedy, G. Murphy, E. Reynolds, M. Avdeev, H. E. R. Brand, and T. Kolodiaznyi, Studies of the antiferrodistortive transition in EuTiO₃, *J. Phys.: Condens. Matter* **26**, 495901 (2014).
- [32] K. Kugimiya, K. Fujita, K. Tanaka, and K. Hirao, Preparation and magnetic properties of oxygen deficient EuTiO_{3-δ} thin films, *J. Magn. Magn. Mater.* **310**, 2268 (2007).
- [33] V. Goian, S. Kamba, J. Hlinka, P. Vaněk, A. A. Belik, T. Kolodiaznyi, and J. Petzelt, Polar phonon mixing in magnetoelectric EuTiO₃, *Eur. Phys. J. B* **71**, 429 (2009).
- [34] N. F. Mott, The transition to the metallic state, *Philos. Mag.* **6**, 287 (1961).
- [35] X. Lin, G. Bridoux, A. Gourgout, G. Seyfarth, S. Krämer, M. Nardone, B. Fauqué, and K. Behnia, Critical Doping for the Onset of a Two-Band Superconducting Ground State in SrTiO_{3-δ}, *Phys. Rev. Lett.* **112**, 207002 (2014).
- [36] P. P. Edwards and M. J. Sienko, Universality aspects of the metal-nonmetal transition in condensed media, *Phys. Rev. B* **17**, 2575 (1978).
- [37] P. P. Edwards, T. V. Ramakrishnan, and C. N. R. Rao, The metal-nonmetal transition: A global perspective, *J. Phys. Chem.* **99**, 5228 (1995).
- [38] S. H. Wemple, Some Transport Properties of Oxygen-Deficient Single-Crystal Potassium Tantalate (KTaO₃), *Phys. Rev.* **137**, A1575 (1965).
- [39] H. Uwe, J. Kinoshita, K. Yoshihiro, C. Yamanouchi, and T. Sakudo, Evidence for light and heavy conduction electrons at the zone center in KTaO₃, *Phys. Rev. B* **19**, 3041 (1979).
- [40] X. Lin, C. W. Rischau, L. Buchauer, A. Jaoui, B. Fauqué, and K. Behnia, Metallicity without quasi-particles in room-temperature strontium titanate, *npj Quantum Mater.* **2**, 41 (2017).
- [41] K. A. Müller, W. Berlinger, and F. Waldner, Characteristic Structural Phase Transition in Perovskite-Type Compounds, *Phys. Rev. Lett.* **21**, 814 (1968).
- [42] Q. Tao, B. Loret, B. Xu, X. Yang, C. W. Rischau, X. Lin, B. Fauqué, M. J. Verstraete, and K. Behnia, Nonmonotonic anisotropy in charge conduction induced by antiferrodistortive transition in metallic SrTiO₃, *Phys. Rev. B* **94**, 035111 (2016).
- [43] A. S. Mishchenko, L. Pollet, N. V. Prokof'ev, A. Kumar, D. L. Maslov, and N. Nagaosa, Polaron mobility in the "beyond quasiparticles" regime, [arXiv:1812.10336](https://arxiv.org/abs/1812.10336).
- [44] J.-J. Zhou, O. Hellman, and M. Bernardi, Electron-Phonon Scattering in the Presence of Soft Modes and Electron Mobility in SrTiO₃ Perovskite from First Principles, *Phys. Rev. Lett.* **121**, 226603 (2018).
- [45] A. Sakai, T. Kanno, S. Yotsuhashi, H. Adachi, and Y. Tokura, Thermoelectric Properties of Electron-Doped KTaO₃, *Jpn. J. Appl. Phys.* **48**, 097002 (2009).
- [46] In the three-band model of van der Marel *et al.* [15] the lowest band is heavy, while the others are light. However, in our much simpler model with purely parabolic bands, we neglect band repulsion. Thus, the second band is the heavy one and crosses the lighter first band.
- [47] J. H. Barrett, Dielectric Constant in Perovskite Type Crystals, *Phys. Rev.* **86**, 118 (1952).
- [48] J. C. Maxwell, *A Treatise on Electricity and Magnetism*, 3rd ed. (Dover, New York, 1954).
- [49] P. Lunkenheimer, V. Bobnar, A. V. Pronin, A. I. Ritus, A. A. Volkov, and A. Loidl, Origin of apparent colossal dielectric constants, *Phys. Rev. B* **66**, 052105 (2002).
- [50] D. Niermann, F. Waschkowski, J. de Groot, M. Angst, and J. Hemberger, Dielectric Properties of Charge-Ordered LuFe₂O₄

- Revisited: The Apparent Influence of Contacts, *Phys. Rev. Lett.* **109**, 016405 (2012).
- [51] J. Hemberger, M. Nicklas, R. Viana, P. Lunkenheimer, A. Loidl, and R. Böhmer, Quantum paraelectric and induced ferroelectric states in SrTiO₃, *J. Phys.: Condens. Matter* **8**, 4673 (1996).
- [52] R. D. Shannon, Revised effective ionic radii and systematic studies of interatomic distances in halides and chalcogenides, *Acta Crystallogr., Sect. A: Found. Adv.* **32**, 751 (1976).
- [53] J. Brous, I. Fankuchen, and E. Banks, Rare earth titanates with a perovskite structure, *Acta Crystallogr.* **6**, 67 (1953).